TUrBO: the Next 100,000+ RPM Synchronous Reluctance Drives

IEEE Open Journal of
Industry Applications

Received 20 April 2026; revised 6 August 2026; accepted 14 August 2026. Date of publication 17 August 2026;
date of current version 11 September 2026.

Digital Object Identifier 10.1109/OJIA.2026.3724749

TUrBO: The Next 100 000^{+} RPM Synchronous Reluctance Drives

YULONG CUI [1] (Graduate Student Member, IEEE), ANDREA CAVAGNINO [1] (Fellow, IEEE), ANDREA TONOLI [2], CHIARA GIANASSI [3], ALESSANDRO FORTUNATO[3], ALESSANDRO ASCARI [3], ERICA LIVERANI[3], DEEKSHITHA SRINIVAS NAYAK [4] (Member, IEEE), GABRIELE RIZZOLI [4] (Member, IEEE), MICHELE MENGONI [4] (Senior Member, IEEE), AND LUCA ZARRI [4] (Senior Member, IEEE)

[1]Dipartimento Energia 'G. Ferraris,' Politecnico di Torino, 10129 Torino, Italy
[2]Dipartimento di Ingegneria Meccanica e Aerospaziale, Politecnico di Torino, 10129 Torino, Italy
[3]Department of Industrial Engineering (DIN), University of Bologna, 40126 Bologna, Italy
[4]Department of Electrical, Electronic, and Information Engineering "G. Marconi," University of Bologna, 40126 Bologna, Italy

CORRESPONDING AUTHOR: Andrea Cavagnino (e-mail:andrea.cavagnino@polito.it).

This work was supported by the European UnionNext Generation EU within the PRIN 2022 program through the TUrBO: the next 100000+rpm synchronous reluctance motor drives project, under Grant D.D. 104 - 02/02/2022 Ministero dell'Università e della Ricerca.

ABSTRACT Ultrahigh-speed electric drives operating beyond 100 krpm are attracting increasing interest in compact turbomachinery and electrified auxiliary systems. Although synchronous reluctance machines represent an attractive permanent-magnet (PM)-free solution, their extension to this operating range is simultaneously constrained by rotor mechanical integrity, converter voltage capability, and the strong interaction between electromagnetic design, manufacturing accuracy, and drive operation. This article presents an integrated system-level approach for the development and experimental validation of a 100 krpm-class synchronous reluctance drive based on the coordinated use of two complementary enabling technologies: a multimaterial axially laminated anisotropic rotor manufactured by laser-directed energy deposition and an open-end winding dual-inverter architecture. The complete development process is presented, including additive-manufacturing technology selection, material characterization, rotor fabrication, electromagnetic and mechanical design, converter implementation, and multidisciplinary optimization. Two prototype drives were developed and experimentally investigated. The machine validation comprises flux-linkage mapping, apparent inductance evaluation, maximum torque-per-ampere assessment, load tests, and acoustic measurements, while the comparison between experiments and finite-element analysis highlights the influence of manufacturing-related phenomena, including the diffusion region generated between adjacent deposited materials. The drive validation further assesses the proposed converter architecture under very-high-speed operating conditions. The presented results demonstrate that the coordinated design of the synchronous reluctance machine, additive-manufacturing process, and power converter is the key enabler of next-generation ultrahigh-speed PM-free electric drives.

INDEX TERMS Additive manufacturing (AM), dual-inverter drives, electric drives, electric machines, experimental validation, finite element analysis, high-speed synchronous reluctance machines (SynRM), open-end winding machines.

I. INTRODUCTION

Very-high-speed electric drives operating in the 100–200 krpm range are attracting increasing interest in compact turbomachinery and electrified auxiliary systems, including compressors, fuel-cell air supply units, aerospace subsystems, turbomolecular pumps, and high-speed industrial equipment [1], [2]. Increasing the rotational speed allows the required power to be obtained from a smaller active volume, but simultaneously intensifies several coupled design constraints.

Centrifugal stresses and rotor-dynamic stability become primary mechanical limitations, while the increased electrical frequency raises stator and rotor losses, converter voltage

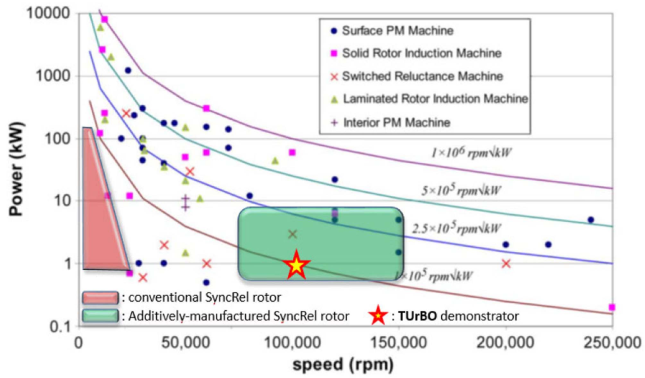

FIGURE 1. Electrical machine topologies for high-speed applications and positioning of the TUrBO drive in the power-speed plane [1].

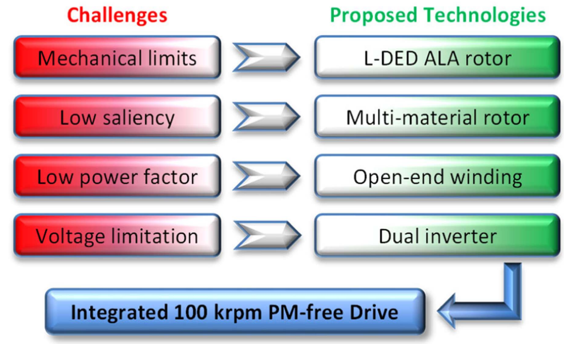

FIGURE 2. Conceptual overview of the proposed integrated 100 krpm PM-free SynRM drive, highlighting the complementary roles of the multimaterial ALA rotor and the open-end winding dual-inverter architecture.

demand, and thermal-management requirements [3]. Consequently, ultrahigh-speed drives must be conceived through a multidisciplinary approach in which the electrical machine, the power converter, the manufacturing process, and the control strategy are developed as a single integrated system rather than as independent subsystems. The positioning of the proposed drive with respect to other high-speed electrical-machine technologies is shown in Fig. 1.

Permanent-magnet (PM) machines currently dominate this operating range owing to their high efficiency, torque density, and wide constant-power capability [4]. Their use, however, introduces dependence on critical raw materials, as well as issues related to cost volatility, supply-chain resilience, magnet retention, and thermal demagnetization [5], [6]. These limitations have stimulated increasing interest in PM-free alternatives. Solid-rotor induction machines are among one of the most established solutions for high-speed compressors and blowers because of their mechanically robust, monolithic rotor and simple construction [1]. Their performance is nevertheless penalized by slip, significant rotor eddy-current losses, and relatively low power factor, which increase both thermal-management and converter requirements. Switched-reluctance machines provide a similarly robust magnet-free rotor but generally suffer from pronounced torque ripple, acoustic excitation, and demanding current control at high electrical frequency.

Synchronous reluctance machines (SynRMs) constitute an attractive PM-free alternative because they combine synchronous operation with the absence of both PMs and rotor windings. Their extension to rotational speeds approaching 100 krpm is, however, far from straightforward. Conventional transversely laminated rotors generate magnetic saliency through internal flux barriers separated by thin structural ribs, resulting in limited mechanical robustness and practical operating speeds typically restricted to a few tens of thousands of revolutions per minute [7]. Replacing the conventional rotor with a multimaterial axially laminated anisotropic (ALA) structure manufactured by laser directed energy deposition (L-DED) substantially improves structural integrity while preserving the magnetic anisotropy required for reluctance torque production [8], [9], [10], an approach also pursued with laser powder bed fusion (LPBF) on solid rotor geometries [11], [12]. Nevertheless, a mechanically robust rotor alone is insufficient to enable practical ultrahigh-speed SynRM operation. At high electrical frequency, the inherently low-power factor of SynRMs increases both converter current and voltage demand, thereby limiting the achievable torque and the constant-power operating range.

The central hypothesis investigated in this work is that practical operation beyond 100 krpm can only be achieved through the coordinated integration of two complementary enabling technologies, illustrated in Fig. 2. The first is a multimaterial L-DED ALA rotor employing FeSi2.9 magnetic layers and AISI 316L nonmagnetic layers to overcome the structural limitations of conventional SynRM rotors. The second is an open-end winding stator supplied by a dual-inverter architecture in which the auxiliary converter provides reactive-power support and additional voltage capability through a floating-capacitor bridge. Neither technology is sufficient in isolation; their coordinated design enables a practical ultrahigh-speed PM-free drive. The interaction between these two subsystems extends well beyond their individual functions. Rotor geometry, deposited-material properties, and manufacturing-induced nonidealities determine the flux-linkage maps, magnetic saliency, torque-per-ampere capability, and reactive-power demand, which directly influence converter voltage utilization, modulation strategy, and current control. Conversely, converter voltage limits and control constraints affect the usable operating region and, in turn, influence the electromagnetic design targets. The proposed system must therefore be regarded as an integrated drive rather than as an electrical machine followed by an independent power converter.

The research presented in this article was carried out within the PRIN 2022 project *TUrBO: the next 100000+ rpm synchronous reluctance motor drives*, whose objective was the experimental demonstration of a PM-free drive operating beyond 100 krpm. Rather than reproducing the individual outcomes of the project as a chronological development report, the present article consolidates its principal scientific results into a unified system-level perspective, complemented by the final experimental validation of the two prototypes.

The main contributions of the article are summarized as follows. First, it presents the integrated conception and experimental validation of a 100 krpm-class PM-free SynRM drive based on the coordinated use of a bimetallic L-DED ALA rotor and an open-end winding dual-inverter architecture. Second, it quantifies the influence of manufacturing-specific nonidealities—including layer-thickness deviations, the measured permeability of deposited AISI 316L, and the FeSi2.9/AISI 316L diffusion region—on the electromagnetic behavior of the machine, thereby directly linking additive-manufacturing accuracy to drive-level performance. Third, it experimentally verifies the mechanical feasibility of the proposed quasisolid rotor architecture and compares two rotor realizations. Fourth, it demonstrates the capability of the floating-capacitor bridge to provide reactive-power compensation and voltage support, enabling the main inverter to operate close to unity power factor. Finally, it presents a comprehensive experimental validation including flux-linkage and apparent inductance mapping, maximum torque-per-ampere (MTPA) operation, load tests, and complete drive operation up to 100 krpm.

The rest of this article is organized as follows. Section II introduces the system-level drive concept and the complementary roles of the multimaterial ALA rotor and the open-end winding dual-inverter architecture. Section III describes the prototype development and manufacturing process. Section IV presents the electromagnetic and mechanical design together with the corresponding finite-element validation. Sections V report the experimental validation of the machine and of the complete drive. Section VI discusses TUrBO power converter and drive control. Finally, Section VII concludes this article.

II. SYSTEM-LEVEL DRIVE CONCEPT

The proposed ultrahigh-speed drive combines two complementary enabling technologies that jointly overcome the principal limitations preventing synchronous reluctance machines from operating beyond 100 krpm. The first addresses the mechanical robustness of the rotor through a multimaterial additively manufactured ALA structure, whereas the second extends the electrical operating range by means of an open-end winding dual-inverter architecture providing reactive-power support and enhanced voltage utilization. Their coordinated operation constitutes the system-level concept investigated in this work.

A. MULTIMATERIAL ALA ROTOR

Among the rotor topologies proposed for high-speed synchronous reluctance machines, ALA structures offer an attractive compromise between magnetic saliency and mechanical robustness. Unlike conventional transversely laminated rotors, where saliency is generated through internal flux barriers separated by thin structural ribs, ALA rotors produce magnetic anisotropy by alternating magnetic and nonmagnetic layers

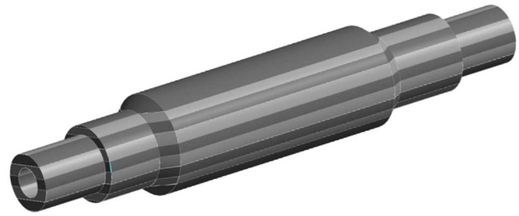

FIGURE 3. Conceptualization of the proposed two-pole ALA rotor. Magnetic layers in dark, nonmagnetic layers in light gray.

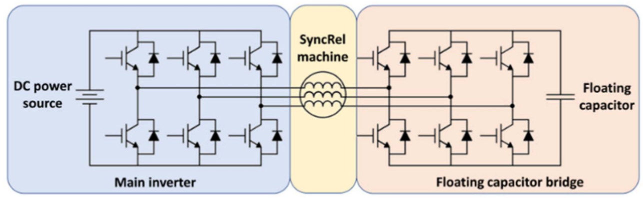

FIGURE 4. Electric drive for a SynRM with open-end winding.

along the shaft axis. This architecture preserves the reluctance torque production mechanism while substantially improving the structural continuity of the rotor [13].

The concept adopted in this work is illustrated in Fig. 3. The rotor consists of alternating FeSi2.9 magnetic layers, which guide the flux along the d-axis, and AISI 316L nonmagnetic layers, which reduce the q-axis permeance and generate the magnetic saliency required for torque production. The proposed rotor is manufactured by L-DED, which enables both materials to be deposited within a single metallurgically bonded component.

Besides simplifying the realization of the ALA architecture, this process introduces manufacturing-specific phenomena—including layer-thickness deviations and the finite diffusion region between adjacent materials—that directly influence the electromagnetic behavior of the machine. Their impact is experimentally quantified in the following sections.

B. OPEN-END WINDING DUAL-INVERTER ARCHITECTURE

Although the proposed rotor overcomes the structural limitations of conventional SynRM rotors, it does not remove the voltage constraints associated with high electrical frequency. To address these limitations, the stator windings are supplied through the open-end winding architecture shown in Fig. 4.

The primary inverter is connected to the main dc source and supplies the active power required by the machine, whereas the secondary inverter incorporates a floating-capacitor bridge that provides reactive-power compensation and additional voltage capability. Compared with a conventional single-inverter solution, this architecture improves dc-link voltage utilization, extends the constant-power operating range, and enables the main inverter to operate close to unity power factor.

These characteristics become increasingly beneficial as the operating speed approaches 100 krpm, where the low power factor of synchronous reluctance machines would otherwise impose severe converter voltage limitations.

C. MACHINE–DRIVE INTERACTION

The proposed drive is based on the premise that neither the rotor nor the converter alone is sufficient to enable practical ultrahigh-speed SynRM operation. Rotor geometry, magnetic saliency, and manufacturing-induced nonidealities determine the flux-linkage maps, torque-per-ampere capability, and reactive-power demand, which directly influence converter voltage utilization and current control. Conversely, converter voltage limits define the usable operating region and therefore become part of the electromagnetic design process.

Consequently, the machine and the converter have been conceived as two strongly coupled subsystems whose coordinated optimization determines the overall drive performance. This system-level approach guided the prototype development presented in the following sections and is experimentally validated through both machine-level and drive-level investigations.

III. DEVELOPMENT OF THE DRIVE PROTOTYPE

The proposed system-level drive concept was experimentally implemented by developing two prototype drives representative of very-high-speed auxiliary applications. Each demonstrator targets approximately 1 kW at 100 000 r/min (100 mNm) and was conceived to validate the proposed combination of a multimaterial additively manufactured ALA rotor and an open-end winding dual-inverter architecture. While the electromagnetic, mechanical, and converter designs are discussed in the following sections, this chapter focuses on the realization of the prototype, including the selection of the manufacturing process, the constituent materials, their characterization, and the fabrication of the bimetallic rotor.

Both demonstrators employ the same stator, housing, cooling system, bearings, resolver, and power-electronic architecture. Consequently, the influence of the rotor design and manufacturing process can be experimentally assessed while maintaining identical electrical and mechanical boundary conditions.

A. ADDITIVE MANUFACTURING (AM) TECHNOLOGY SELECTION

The realization of the proposed multimaterial ALA rotor requires a manufacturing technology capable of producing alternating magnetic and nominally nonmagnetic layers while ensuring adequate metallurgical bonding, sufficient mechanical integrity, and acceptable dimensional accuracy. Among the currently available metal AM technologies, L-DED was selected as the most suitable solution for the proposed rotor architecture. The principal requirement is the reliable alternation of two metallic materials within the same component while preserving interfacial continuity. In LPBF, multimaterial fabrication requires repeated powder replacement, chamber cleaning, and strict cross-contamination control, making frequent alternation of materials impractical. By contrast, L-DED enables material switching simply by changing the delivered powder stream while simultaneously offering substantially higher deposition rates. Although the achievable geometrical resolution is lower than that of LPBF (typically 1–1.5 mm), this limitation is acceptable because the final rotor dimensions are obtained through subsequent turning and grinding operations rather than by the as-built geometry.

Compared with other layered manufacturing approaches, L-DED also provides a favorable compromise between manufacturing flexibility and dimensional accuracy. Wire arc AM, conceptually similar to L-DED, deposits material by melting a metallic wire with an electric arc. Although suitable for large structural components, its relatively coarse deposition resolution makes it less appropriate for the thin alternating layers required by the proposed ALA rotor. A wire-fed L-DED solution could potentially provide even finer layers than the adopted powder-fed process; however, commercial FeSi alloy wires are currently unavailable. Consequently, powder-fed L-DED was selected as the best compromise between achievable geometrical precision, material availability, and manufacturing flexibility.

Hot isostatic pressing (HIP) could also be employed after deposition to reduce residual porosity and further increase design flexibility. However, metallographic observations performed on the manufactured specimens confirmed crack-free deposits with relative densities above 99.4% for both FeSi2.9 and AISI 316L, as well as excellent metallurgical bonding between adjacent layers [14]. Under these conditions, HIP was considered unnecessary for the present prototypes. The remaining limitation intrinsic to the L-DED process is the formation of a finite interfacial diffusion region between the two deposited materials. As discussed later, this diffusion region influences the electromagnetic behavior of the rotor and therefore represents an integral part of the proposed system-level design rather than merely a manufacturing imperfection.

B. MATERIAL SELECTION

The selection of the constituent materials was driven by a combination of electromagnetic, mechanical, and manufacturing requirements. Besides providing the magnetic anisotropy required for reluctance torque production, the selected materials had to be compatible with the L-DED process, exhibit comparable thermo-mechanical behavior, and withstand the severe centrifugal stresses associated with operation at 100 krpm.

The flux-guide (FG) material requires high magnetic permeability, low electrical conductivity, and adequate processability by L-DED. Fe–Si alloys containing approximately 2.5–3.5 wt.% silicon represent a suitable compromise between magnetic performance and manufacturability; consequently, FeSi2.9 was selected as the magnetic material [12]. For the flux-barrier (FB) material, nearly paramagnetic behavior, low electrical conductivity, and good metallurgical compatibility with the magnetic alloy are desirable. Austenitic stainless steel AISI 316L was therefore selected owing to its robust L-DED processability and favorable mechanical properties [15], [16].

TABLE 1. Parameters for the Materials Used in the Bimetallic Rotor Preform

Material	Scan velocity v [**mm/min**]	Laser power P [**W**]	Powder flow rate g [**g/min**]
AISI 316L	1020	2200-2000-80	9.1
FeSi 2.9%	1200	2000-1800-80	10

Alternative candidate materials, including FeSi6.5, FeCo50, and Ti6Al4V, were also evaluated during the preliminary design phase. However, they were not adopted because the corresponding L-DED process was insufficiently mature or, in the case of FeCo50, because of excessive porosity observed during preliminary manufacturing trials.

The FeSi2.9/316L material pair also provides favorable mechanical compatibility. Their similar densities (approximately 7700 and 7850 kg·m^{-3}, respectively) reduce the sensitivity of the rotor to layer-thickness deviations, while the thermal-expansion mismatch, although not negligible, remains compatible with the proposed quasisolid rotor architecture and is explicitly considered in the structural assessment presented in Section IV.

Two commercially available gas-atomized powders were finally selected: FeSi2.9 (m4p Material Solutions GmbH, Austria, particle size 45–106 μm) and AISI 316L (Heeger Materials Inc., USA, particle size 53–150 μm).

C. MATERIAL CHARACTERIZATION

Following the selection of the constituent materials, a comprehensive experimental characterization was carried out to determine the mechanical and magnetic properties required for the subsequent electromagnetic and structural design activities. Since the final rotor properties are strongly affected by the additive-manufacturing process, all measurements were performed on specimens manufactured using the same L-DED equipment, process parameters, and postprocessing conditions adopted for the prototype rotors.

The deposition parameters employed for both materials are summarized in Table 1. Because alloy-specific heat treatments are impractical in a multimaterial component, all specimens were subjected to a common postdeposition thermal treatment consisting of one hour at 850 °C followed by air cooling. This treatment improves the magnetic behavior of FeSi2.9 while simultaneously relieving residual stresses within the AISI 316L phase.

Mechanical characterization was carried out on both single-material and bimetallic specimens machined by wire electrical discharge machining according to BS EN ISO 6892. The strain was measured using a conventional extensometer for the single-material specimens and digital image correlation for the bimetallic specimens. The corresponding engineering stress–strain curves are reported in Fig. 5, whereas the resulting mechanical properties are summarized in Table 2.

The obtained results confirm that both constituent materials exhibit mechanical properties compatible with the proposed rotor architecture while maintaining adequate metallurgical

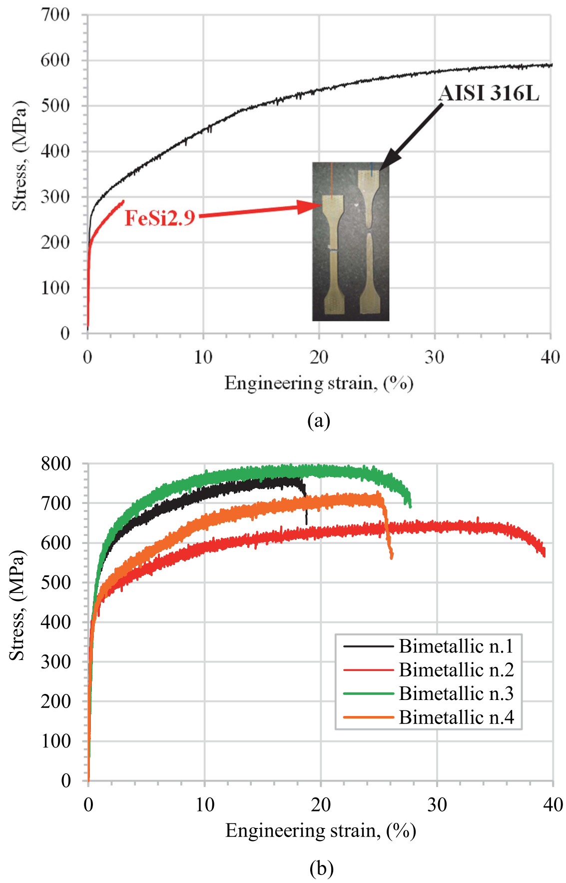

FIGURE 5. Engineering stress-strain curves obtained from tensile tests on (a) Single-material specimens and (b) Bimetallic specimens.

TABLE 2. List of Mechanical Properties Obtained From Tensile Tests

Specimen	Yield strength $R_{P0.2}$ [MPa]	Ultimate tensile strength UTS [MPa]	Max strain ε_{ext} [%]	Max strain – DIC ε_{DIC} [%]
FeSi2.9 – Test 1	215	255	1.1	–
FeSi2.9 – Test 2	190	290	3.1	–
316L – Test 1	190	470	44.0	–
316L – Test 2	230	555	44.2	–
Bimetallic n. 1	297	782	18.8	16.2
Bimetallic n. 2	343	665	39.2	39.9
Bimetallic n. 3	267	798	27.7	29.3
Bimetallic n. 4	313	730	26.2	25.3

bonding at the material interfaces. The bimetallic specimens also demonstrate that the deposition process does not introduce significant defects that could compromise the structural integrity of the rotor.

Magnetic characterization was performed on annealed toroidal specimens manufactured using the same L-DED process as the rotor blanks. The measurements were conducted in accordance with EN IEC 60404-6:2018 using dedicated excitation and sensing windings. The resulting magnetization curves, hysteresis loops, and specific iron losses are summarized in Fig. 6.

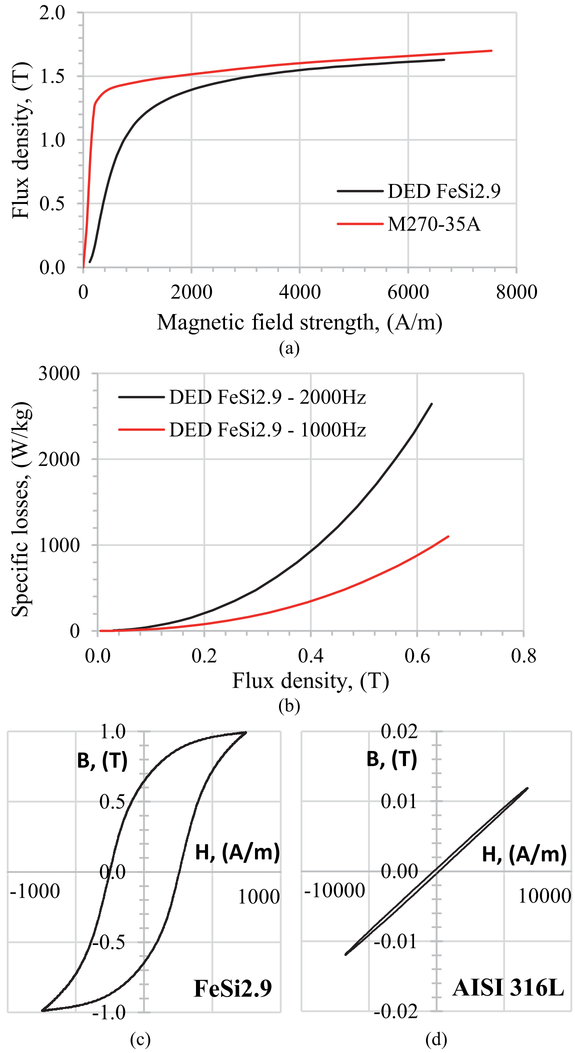

FIGURE 6. **Magnetic characterization results: (a) Magnetization *B–H* curve of FeSi2.9 at 1 Hz, with M270-35A shown for reference; (b) Specific loss of FeSi2.9 at 1000 Hz and 2000 Hz; (c) Hysteresis loop of FeSi2.9 at 1 T and 1 Hz; and (d) Hysteresis loop of AISI 316L at 1 Hz.**

The measured magnetic properties reveal two aspects of particular importance for the subsequent electromagnetic design. First, the deposited FeSi2.9 exhibits magnetic characteristics suitable for reluctance-machine applications, although slightly inferior to those of conventional rolled electrical steels due to the additive-manufacturing process. Second, the measured relative permeability of the deposited AISI 316L is significantly higher than the value commonly reported for wrought material. Since this parameter directly influences the magnetic reluctance of the flux barriers, the experimentally measured permeability is adopted throughout the electromagnetic analysis presented in the following sections.

D. BIMETALLIC ROTOR FABRICATION

Following the material characterization, the rotor preforms were manufactured using the selected L-DED process. The adopted fabrication strategy combines AM with conventional

FIGURE 7. **DED system used for bimetallic preform fabrication: robotic deposition platform (left) and dual-material powder-feeding system (right).**

FIGURE 8. **Fabrication sequence: as-built multilayer block, intermediate cylindrical preform, and finish-machined rotor.**

machining to exploit the design flexibility of L-DED while achieving the dimensional accuracy required for ultrahigh-speed operation.

The manufacturing system employed for the deposition process is shown in Fig. 7. The robotic L-DED platform is equipped with two independent powder feeders that alternately deliver FeSi2.9 and AISI 316L, enabling the sequential deposition of magnetic and nonmagnetic layers within a single metallurgically bonded component.

The adopted fabrication sequence is illustrated in Fig. 8. The process starts with an oversized multilayer prismatic block, which is subsequently machined into an intermediate cylindrical preform, after which the final rotor geometry is obtained by precision turning and grinding. This hybrid manufacturing strategy exploits the flexibility of AM while relying on conventional machining to achieve the dimensional tolerances, concentricity, and surface quality required for operation at 100 krpm.

The proposed approach is compatible with both monolithic rotors incorporating the shaft journals and rotors assembled by interference fitting. In the present work, the manufacturing route follows an "additive preform + subtractive finishing" philosophy, where L-DED is employed to generate the bimetallic architecture and the final dimensions are imposed through conventional machining.

The first manufactured rotor (Prototype 1) highlighted the sensitivity of the electromagnetic behavior to the dimensional deviations intrinsically associated with the deposition process. Based on these observations, the manufacturing route was refined by introducing interlayer grinding between successive deposition steps, significantly improving control over layer thicknesses and enabling the realization of thinner nonmagnetic regions [17]. This refinement was adopted for the fabrication of Prototype 2 and constitutes one of the principal manufacturing improvements investigated in the present work.

With the improved manufacturing procedure, the average layer-thickness deviation was reduced to approximately ±0.3 mm, considerably improving the geometrical fidelity of the manufactured rotor. Nevertheless, the remaining manufacturing deviations and the finite diffusion region generated between adjacent deposited materials remain important characteristics of the L-DED process. The metallurgical mechanisms responsible for the formation of this interfacial region are discussed in detail in [18], whereas its influence on the electromagnetic behavior of the machine is addressed in the following sections.

IV. SYNRM DESIGN AND FEM-BASED VALIDATION

The development of the proposed prototype required the simultaneous optimization of the electromagnetic, mechanical, thermal, and manufacturing aspects introduced in the previous sections. Unlike conventional electrical-machine design, where the electromagnetic performance can often be optimized independently of the manufacturing process, the proposed multimaterial ALA rotor establishes a strong interaction among geometry, material properties, structural integrity, and converter operating conditions. Consequently, the machine was designed through a multidisciplinary approach in which electromagnetic, mechanical, and manufacturing considerations were iteratively refined before the experimental validation of the final prototypes [19].

A. ELECTROMAGNETIC DESIGN

The proposed drive targets approximately 1 kW at 100 000 r/min (100 mNm), representative of very-high-speed auxiliary applications such as compressors, fuel-cell air supply units, and turbomachinery auxiliaries. Starting from the system-level concept introduced in Section II, the electromagnetic design aimed at maximizing torque density while simultaneously satisfying the structural and manufacturing constraints imposed by the L-DED rotor technology.

Additively manufactured ALA rotors combine the mechanical robustness of a quasisolid rotor with the magnetic anisotropy required to produce reluctance torque [8], [20].

TABLE 3. Main Design Parameters of the SynRM Prototype

Rated power, (W)	1050
Rated speed, (rpm)	100,000
Rated torque, (Nm)	0.1
Number of poles	2
Rated phase voltage, (V)	200
Stator outer diameter, (mm)	45
Rotor outer diameter, D_{ro} (mm)	21
Active stack length, L_{stk} (mm)	50
Air-gap length, (mm)	0.25
Number of stator slots	18
Slots per pole per phase	3
Series turns per phase	66
Turns per coil	11
Wire diameter, (mm)	0.5
Winding layout	double layer, 2-slot short pitch
Measured stator resistance @ 20 ℃	1.36/1.37Ω (prot. 1/prot. 2)
End-winding leakage, (mH)	0.0956 mH
Number of rotor layers	10
FG/FB	$FeSi_{2.9\%}$ / AISI 316L
Cooling	water jacket, 1.5 L/min
Inlet water temperature, (°C)	≈20–25
Bearings	HY KH 6001 C TA, 12 mm bore

A two-pole topology was selected to reduce the fundamental electrical frequency, thereby limiting stator core losses, rotor eddy-current losses, and converter switching constraints. The rated phase voltage was set to around 200 V to maintain moderate phase currents while remaining compatible with the proposed open-end winding dual-inverter architecture.

The preliminary machine dimensions were obtained from the conventional sizing (1), where D_{ro} is the rotor outer diameter, L_{stk} the active stack length, $D_r$the rated torque, η the efficiency, PF the power factor, k_w the winding factor, A the electrical loading, and $B_g$the peak air-gap flux density [21].

$$D_{\text{ro}}^2 L_{stk} = \frac{T_r}{\left(\frac{\pi}{2\sqrt{2}}\right) k_{w1,s} \left(\eta \cos\varphi\right) A B_g}. \tag{1}$$

For the initial sizing, conservative design values were adopted for magnetic and electrical loading, efficiency, and power factor, while the aspect ratio was maintained below three to avoid higher order critical speeds [22].

The resulting machine employs an 18-slot stator with a double-layer distributed winding, 66 series turns per phase, and a two-slot short pitch. The main machine-design parameters are summarized in Table 3.

The proposed two-pole ALA rotor is illustrated in Fig. 9, where the dimensions of the magnetic (FG) and nonmagnetic (FB) layers are indicated.

The stator is integrated within the water-jacket housing shown in Fig. 10, which was specifically developed for continuous high-speed operation. Although the cooling system is not part of the electromagnetic optimization itself, it enables

TABLE 4. FEM-Predicted Steady-State Performance at the Rated Point for Two 316L Relative Permeabilities, Namely, the Literature-Reported Value $\mu_{r,316L} = 1.02$ and the Value Measured for the DED-Fabricated 316L in This Work $\mu_{r,316L} = 1.4$

$n_{op} = 100$krpm; $\gamma = 45°$; $T_{sw} = 115$°C; $T_r = 90$°C; $T_e = 100$ mNm						
	316L relative permeability, $\mu_{r,316L}$					
	$\mu_r = 1.02$			$\mu_r = 1.40$		
Parameter	Design 1	Proto 1	Design&Proto 2	Design 1	Proto 1	Design&Proto 2
Phase current I_{ph} (A_{rms})	2.91	3.04	2.83	2.94	3.05	2.96
Phase voltage V_{ph} (V_{rms})	205.1	210.4	227.3	211.4	213.5	234.1
Power factor (−)	0.62	0.59	0.57	0.60	0.58	0.54
Magnetic loading B_g (T)	0.41	0.41	0.46	0.43	0.42	0.48
Electric loading A (A/cm)	170.6	178.2	165.9	172.3	178.8	173.5
Current density J (A/mm^2)	14.82	15.48	14.41	14.97	15.53	15.08
Thermal loading AJ (A^2/mm^2/cm)	2528	2759	2391	2581	2778	2616
Torque ripple (%)	30.8	147.7	22.9	29.7	131.1	22.2
Phase resistance R_{ph}@115°C (Ω)	1.904	1.904	1.820	1.904	1.904	1.820
d-axis inductance L_d (mH)	9.34	8.60	10.58	9.50	8.83	10.31
q-axis inductance L_q (mH)	1.46	1.39	2.24	1.75	1.64	2.68
Saliency ratio $\xi = L_d/L_q$ (−)	6.4	6.2	4.7	5.4	5.4	3.9
Stator copper loss $P_{\mathrm{cu,s}}$ (W)	48.4	52.8	43.8	49.4	53.1	47.9
Stator core loss $P_{fe,s}$ (W)	127.6	120.6	99.1	120.4	113.5	98.9
Rotor solid loss $P_{\mathrm{rot,solid}}$ (W)	88.8	94.3	88.6	87.6	92.0	90.9
Total EM losses $P_{\mathrm{loss,EM}}$ (W)	264.8	267.7	231.5	257.4	258.6	237.8
EM efficiency η_{EM} (%)	79.8	79.6	81.9	80.3	80.2	81.5

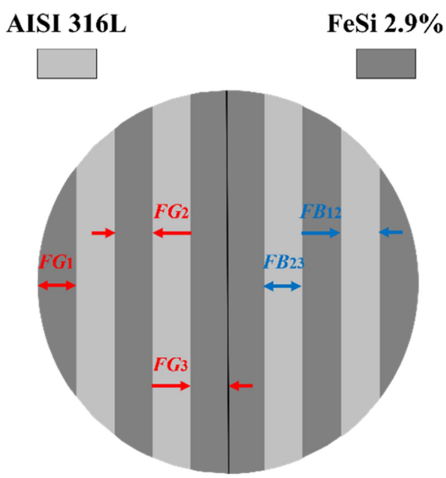

FIGURE 9. Proposed two-pole, ten-layer bimetallic ALA rotor, showing the FG and FB layer-thickness parameters.

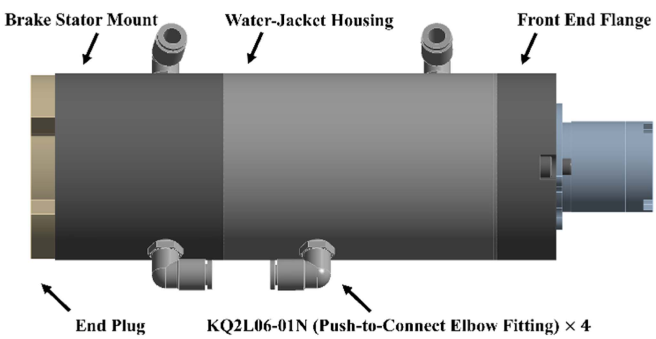

FIGURE 10. TUrBO motor water-jacket housing assembly with coolant-port fittings.

the electrical loading adopted during the design while maintaining the winding temperature below the specified thermal limit.

In the rotor dq reference frame, the electromagnetic torque is expressed as follows:

$$T_e = \frac{3}{2}p\left(\lambda_d i_q - \lambda_q i_d\right). \quad (2)$$

$$\begin{cases} \lambda_d\left(i_d, i_q\right) = \left(L_{dm} + L_\sigma\right) i_d + L_{dq} i_q = L_d i_d + L_{dq} i_q \\ \lambda_q\left(i_d, i_q\right) = L_{dq} i_d + \left(L_{qm} + L_\sigma\right) i_q = L_q i_q + L_{dq} i_d \end{cases}. \quad (3)$$

Neglecting the cross-coupling term, the torque equation simplifies into

$$T_e = \frac{3}{2}p\left(L_d - L_q\right) i_d i_q = \frac{3}{2}pL_d\left(1 - \frac{1}{\xi}\right) i_d i_q \quad (4)$$

These equations highlight that the torque capability of the proposed machine primarily depends on the magnetic saliency generated by the multimaterial ALA rotor [23]. Consequently, the optimization of the layer geometry directly influences not only the electromagnetic performance but also the operating conditions of the entire drive.

The realizable number of layers is constrained by the relatively small rotor diameter together with the geometrical resolution of the L-DED process. A first ten-layer rotor configuration (Design 1) was therefore manufactured and experimentally evaluated. Based on the observed manufacturing tolerances and electromagnetic behavior, a second rotor geometry (Design 2) was subsequently obtained through an evolutionary optimization process to reduce torque ripple and improve overall efficiency [17], [24]. The corresponding manufactured prototypes are compared in Fig. 11.

The electromagnetic performance of both rotor realizations was evaluated using 2-D finite-element analysis under rated operating conditions. Since the magnetic permeability of additively manufactured AISI 316L differs from the value commonly reported for wrought material, two permeability

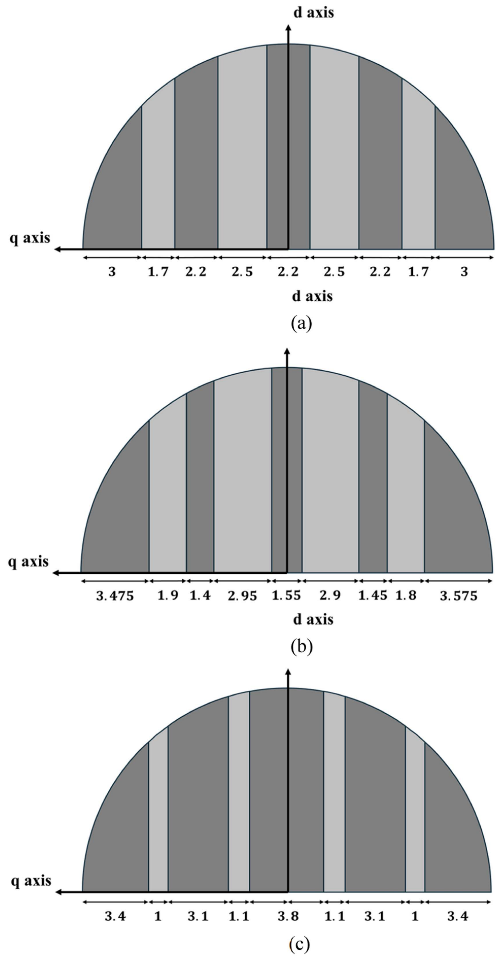

FIGURE 11. Half-cross-sectional views of the TUrBO rotor geometries: (a) Design 1, (b) Prototype 1, and (c) Design 2 / Prototype 2.

TABLE 5. Prototype 1: Steady-State Load Tests

Speed	Torque	CurrentAngle	Winding temp.	Vline,fund	Iline	Pinput	Eff.	PF
rpm	Nm	°	°C	V	A	W	-	-
25 000	0.100	46.0	64.4	52.3	6.010	362.8	0.721	0.627
50 000	0.100	46.0	76.8	101.1	6.057	674.1	0.779	0.603
75 001	0.101	46.0	77.0	147.3	6.129	965.6	0.818	0.597

values were considered during the simulations: the literature value and the experimentally measured value obtained from the L-DED specimens characterized in Section III.

The resulting steady-state electromagnetic predictions are summarized in Table 5. While the FEM model provides a separation of the electromagnetic losses into stator copper, stator core, and rotor solid components, such a separation cannot be obtained experimentally from external electrical measurements, since only the overall machine losses are directly accessible.

B. MECHANICAL AND ROTORDYNAMIC VERIFICATION

At rotational speeds approaching 100 krpm, the mechanical integrity of the rotor becomes one of the primary design constraints. Unlike conventional synchronous reluctance

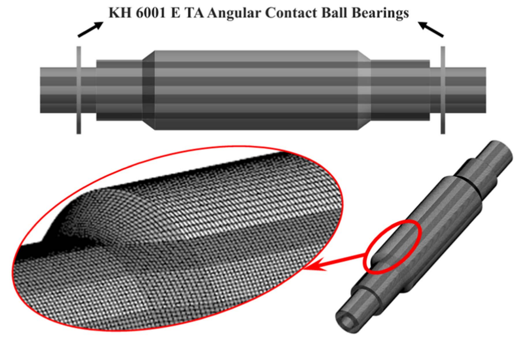

FIGURE 12. 3-D models used for rotor mechanical assessment: Assembled rotor–shaft geometry (top) and finite-element mesh for static-structural analysis (bottom).

machines, where electromagnetic performance often dominates the design process, the proposed quasisolid ALA rotor must simultaneously withstand the severe centrifugal stresses associated with ultrahigh-speed operation while maintaining the magnetic anisotropy required for reluctance torque production.

The structural verification was therefore performed concurrently with the electromagnetic optimization using 3-D finite-element analysis implemented in ANSYS Mechanical. The complete rotor–shaft assembly employed for the structural simulations is shown in Fig. 12.

All interfaces between adjacent deposited materials were modeled as bonded contacts, consistent with the metallurgical bonding produced by the L-DED process. The numerical model comprises approximately 1.06 million finite elements and evaluates the combined effect of centrifugal loading and thermal expansion at both room temperature and the maximum operating temperature considered during the design. The structural assessment considers the different mechanical behavior of the constituent materials.

The ductile AISI 316L layers were evaluated using the von Mises criterion, whereas the FeSi2.9 layers were assessed through the modified Mohr–Coulomb criterion because of their comparatively brittle behavior [25]. A minimum safety factor of 1.5 was adopted throughout the design process.

$$F_{s,v} = \frac{S_{\text{yield}}}{\sigma_v} \tag{5}$$

$$\sigma_v = \sqrt{\frac{(\sigma_r - \sigma_t)^2 + (\sigma_t - \sigma_z)^2 + (\sigma_z - \sigma_r)^2}{2}}. \tag{6}$$

The resulting stress distributions are reported in Fig. 13, which illustrates the radial, tangential, axial, and equivalent von Mises stresses evaluated along the rotor radius at both

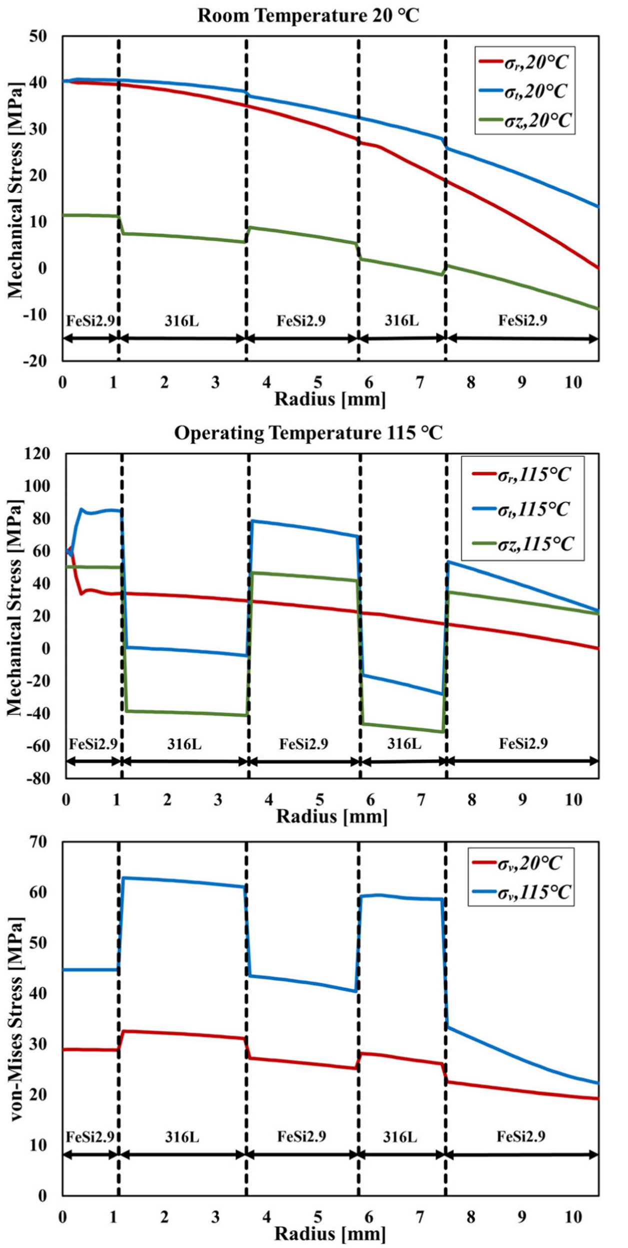

FIGURE 13. Mid-plane stress distributions along the rotor radius: (top) radial, tangential, and axial stresses σ_r, σ_t, and σ_z at room temperature; (middle) σ_r, σ_t, and σ_z at operating temperature; (bottom) von Mises stress σ_v at 20 °C and 115 °C. Dashed lines indicate the FeSi2.9/316L interfaces.

room temperature and operating temperature.

$$F_{s,c} = \begin{cases} \frac{S_{\text{tensile}}}{\sigma_1}, & \sigma_1 \geq \sigma_3 \geq 0 \\ \frac{S_{\text{tensile}}}{\sigma_1}, & \sigma_1 \geq 0 \geq \sigma_3 \; and \; \left|\frac{\sigma_3}{\sigma_1}\right| \leq 1 \\ \frac{S_{\text{com}} S_{\text{tensile}}}{(S_{\text{com}} - S_{\text{tensile}})\sigma_1 - S_{\text{tensile}}\sigma_3}, & \sigma_1 \geq 0 \geq \sigma_3 \wedge \left|\frac{\sigma_3}{\sigma_1}\right| > 1 \\ -\frac{S_{\text{com}}}{\sigma_3}, & 0 \geq \sigma_1 \geq \sigma_3 \,. \end{cases} \quad (7)$$

The simulations indicate that the minimum safety factor remains above two throughout the operating range, confirming the structural suitability of the proposed quasisolid rotor

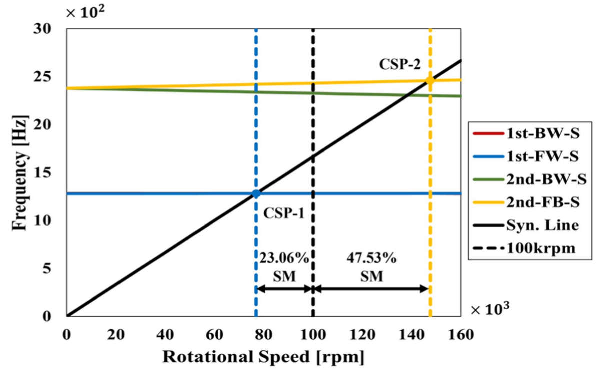

FIGURE 14. Campbell diagram of the studied rotor–bearing system (S: stable, FW: forward whirl, BW: backward whirl, CSP: critical speed point).

architecture. The highest equivalent stresses occur within the AISI 316L layers, particularly under operating-temperature conditions. Although the slightly higher density of AISI 316L contributes to the centrifugal loading, the dominant contribution originates from the thermo-mechanical stresses generated by the different thermal expansion coefficients of the two constituent materials.

Consequently, the thermal behavior of the rotor represents an important design consideration for multimaterial high-speed electrical machines. Because the two materials are metallurgically bonded, the thermo-mechanical analysis explicitly accounts for their temperature-dependent thermal expansion coefficients. The structural solution was obtained by simultaneously applying a centrifugal load at 100 krpm and two uniform body temperatures, namely, 20 °C and 115 °C. The former corresponds to the stress-free reference condition after the common postdeposition heat treatment, whereas the latter represents the winding thermal-protection limit and was adopted as a conservative upper bound for the rotor temperature. The resulting stress concentrations at the $FeSi_{2.9\%}$/AISI 316L interfaces suggest that thermoelastic stresses dominate over the centrifugal contribution in defining the local design margin. Although the predicted minimum safety factor remains above two, the possible degradation of the interfacial bond under repeated thermal cycling is beyond the scope of the present quasistatic structural model and will be the subject of future thermo-mechanical fatigue investigations.

Rotor dynamic behavior was subsequently evaluated to verify the separation between the operating speed and the natural frequencies of the rotor-bearing assembly. The adopted bearing configuration employs high-speed angular-contact ball bearings specifically selected for operation at around 100 krpm. The bearing stiffness adopted in the rotor–bearing model was estimated following [26], [27]. The corresponding Campbell diagram and the first vibration modes are reported in Figs. 14 and 15. The numerical results confirm adequate separation margins between the rated operating speed and the critical speeds of the rotor-bearing system, satisfying the design criteria adopted for ultrahigh-speed rotating machinery.

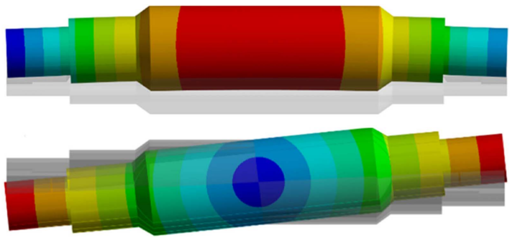

FIGURE 15. Deformation mode shapes of the TUrBO rotor at the critical frequencies: first bending mode (1281 Hz, top) and second bending mode (2379.2 Hz, bottom).

No critical resonance is predicted within the intended operating region, providing additional confidence in the mechanical feasibility of the proposed prototype.

Overall, the combined structural and rotordynamic analyses demonstrate that the proposed multimaterial ALA rotor meets the mechanical requirements of operation at 100 krpm while preserving the electromagnetic architecture necessary for reluctance torque production. The following section experimentally validates the resulting machine through electromagnetic measurements performed on the two manufactured prototypes.

V. SYNRM EXPERIMENTAL VALIDATIONS

The design methodology presented in the previous section was experimentally validated on the two manufactured SynRM prototypes. While the electromagnetic and mechanical analyses demonstrated the feasibility of the proposed multimaterial ALA rotor from a design perspective, experimental validation remains essential, as several manufacturing-related phenomena cannot be accurately predicted by numerical models alone. In particular, dimensional deviations associated with the L-DED process, the actual magnetic properties of the deposited materials, and the diffusion region generated between adjacent layers directly influence the flux-linkage characteristics, the inductance maps, the maximum torque-per-ampere operation, and ultimately the overall machine performance.

To assess these effects, an extensive experimental campaign was carried out on both prototypes. The measurements include flux-linkage mapping, apparent inductance evaluation, comparison with finite-element predictions, investigation of the influence of the interlayer diffusion region, and steady-state and overload capability tests. The resulting measurements provide a comprehensive experimental validation of the proposed machine and establish the basis for the complete drive validation presented in the following section.

A. TEST BENCH

The experimental characterization was carried out using the test bench shown in Fig. 16. Two interchangeable mechanical assemblies were developed for the two SynRM prototypes, while the same power converters, instrumentation, cooling system, resolver interface, and data-acquisition hardware were employed throughout the experimental campaign.

This configuration allows the influence of the two rotor realizations to be experimentally evaluated under identical electrical and mechanical operating conditions.

Although the complete drive proposed in this work employs the open-end winding dual-inverter architecture described in Section II, the experimental characterization presented in this section was performed using conventional three-phase three-level voltage-source converters shown in Fig. 17. This choice allows the intrinsic electromagnetic behavior of the machine to be evaluated independently of the voltage-extension capability and reactive-power compensation provided by the dual-inverter topology. Consequently, the measured flux-linkage maps, inductance maps, MTPA trajectories, and load characteristics can be directly compared with the finite-element predictions presented in Section IV.

The SynRM prototype was mechanically coupled to a PM machine through a precision high-speed shaft. The PM machine was supplied by a separate drive and operated either as a speed-controlled prime mover or as a programmable dynamometer, depending on the specific experimental test. The electrical configurations adopted during the measurement campaign are summarized in Fig. 18. In particular, two operating configurations were adopted during the experimental campaign according to the objectives of the individual tests.

During the flux-linkage mapping experiments, the SynRM prototype operated under current control, whereas the PM machine maintained constant rotational speed. This operating mode allows the complete current plane to be explored under steady-state conditions, enabling accurate measurement of the stator flux-linkage maps over the entire operating region [28].

For the load tests, the operating roles of the two machines were reversed. The SynRM prototype operated under speed control, whereas the PM machine generated the required braking torque by dissipating the recovered mechanical power through a controlled AC/DC converter. This configuration provides superior speed stability during high-load operation and avoids the control limitations associated with torque-controlled operation of the SynRM at elevated load levels [28].

Throughout the machine-characterization campaign, the stator winding was connected in delta to reproduce the electrical configuration adopted during the electromagnetic design and finite-element validation. Voltage, current, torque, speed, and dc-link quantities were simultaneously acquired by the real-time measurement system, providing the experimental data used for the validation presented in the following subsections.

B. FLUX AND INDUCTANCE MAPPING

The electromagnetic characterization of the two SynRM prototypes began with the experimental measurements of the stator flux-linkage maps. These measurements constitute the fundamental experimental dataset from which the apparent inductance maps and the MTPA trajectories are derived. Consequently, the accuracy of the entire electromagnetic

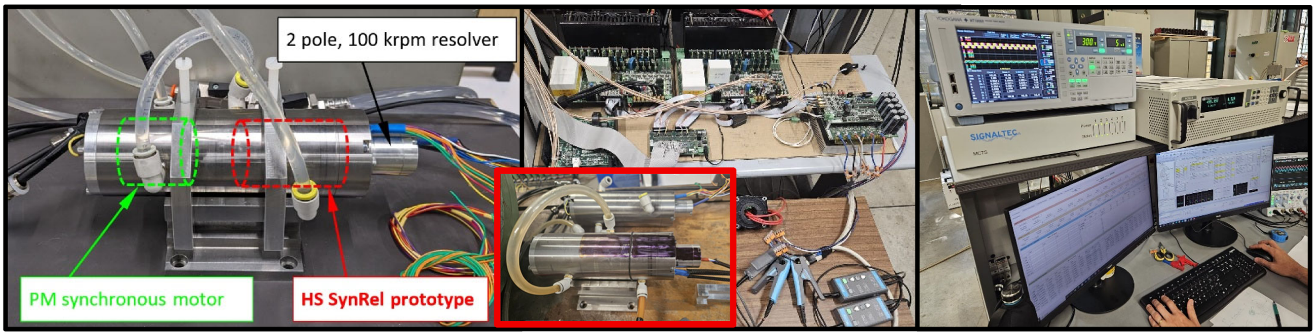

FIGURE 16. Experimental setup for the prototype characterization and load tests: the mechanical test bench with the PM loading machine and the interchangeable high-speed SynRM prototype (left, resolver visible), the power converters (center), and the automated data-acquisition system (right).

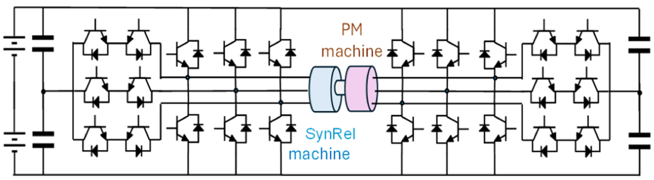

FIGURE 17. Schematic of the experimental drive system, including the two three-level T-type converters.

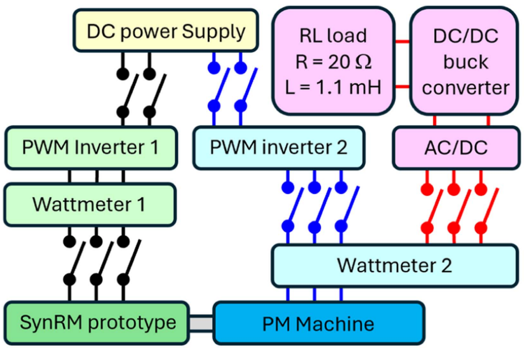

FIGURE 18. Conceptual layout of the test bench used for the flux mapping, no-load tests, and variable-speed load tests.

validation directly depends on the quality of the measured flux-linkage maps.

The flux-linkage maps were experimentally obtained following the measurement procedure described in [29]. During the measurements, the SynRM prototype operated under current control while the PM loading machine maintained constant rotational speed, allowing the complete (i_d, i_q) current plane to be explored under steady-state conditions.

All measurements were performed at 20 krpm, corresponding to approximately one-fifth of the rated speed. This operating condition represents the optimum compromise between measurement accuracy and operating representativeness. At lower speeds, the reduced voltage limits the accuracy of the estimated flux linkages, whereas at higher speeds the increasing influence of current-control dynamics and rotor-position errors introduces nonnegligible current-vector positioning errors, particularly under high-load operating conditions. The selected operating speed therefore ensures accurate and repeatable flux-linkage measurements over the complete current operating region.

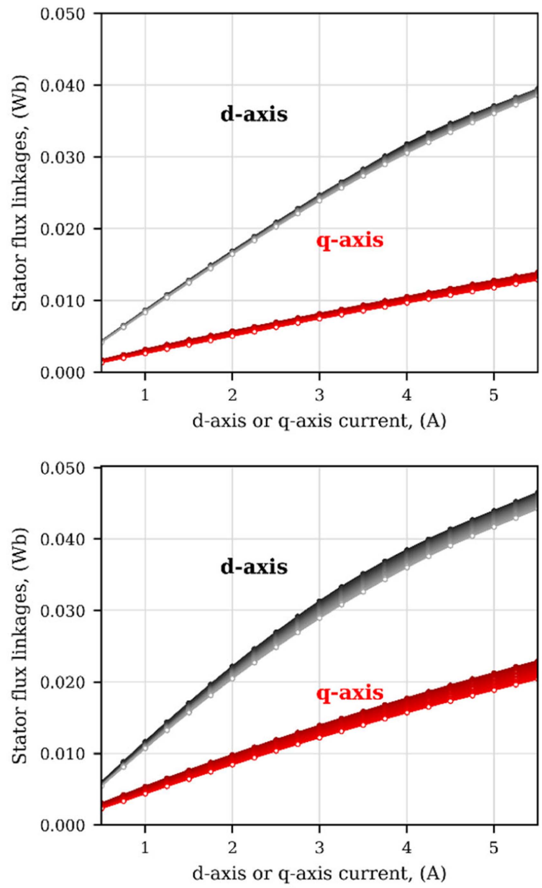

FIGURE 19. Stator flux linkage of prototype 1 (top) and Prototype 2 (bottom). Measurements conducted at 20 krpm.

The measured d-axis and q-axis flux-linkage maps of the two prototypes are reported in Fig. 19. The maps exhibit the characteristic behavior expected for synchronous reluctance machines, with the d-axis flux linkage increasing almost linearly over most of the operating region, while the q-axis flux linkage remains considerably smaller owing to the magnetic anisotropy introduced by the ALA rotor. More importantly,

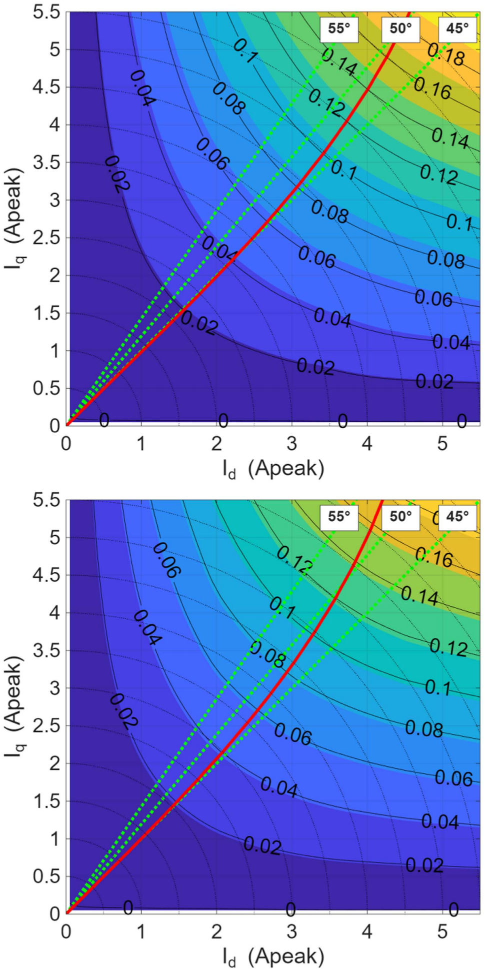

FIGURE 20. MTPA trajectories of Prototype 1 (top) and Prototype 2 (bottom), derived from the experimentally obtained flux-linkage maps.

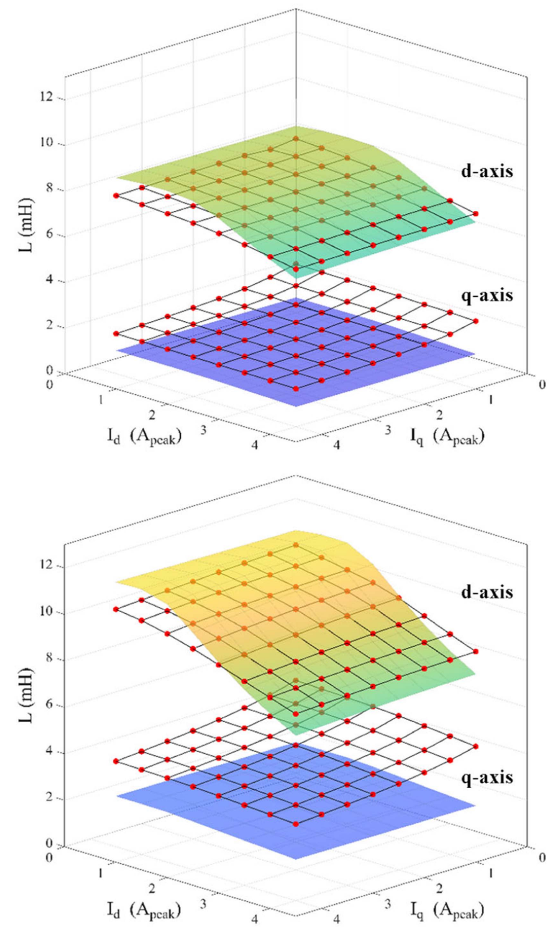

FIGURE 21. Comparison of the measured (red markers) and 2-D FEM-predicted (translucent surfaces) *d*-axis and *q*-axis inductance maps evaluated at 20 krpm: Prototype 1 on the top, and Prototype 2 on the bottom.

the measured flux-linkage maps provide the experimental basis for all the subsequent electromagnetic analyses presented in this work.

The measured flux-linkage maps were subsequently used to derive the experimental MTPA trajectories shown in Fig. 20. Since the MTPA curves are directly calculated from the measured flux-linkage surfaces, they provide a first validation of the global electromagnetic behavior of the two prototypes under optimum current excitation. The experimental trajectories are in good agreement with the finite-element predictions over the entire operating range, confirming that the adopted electromagnetic model accurately reproduces the overall torque-production mechanism of both machines [28].

The same measured flux-linkage maps were finally employed to calculate the apparent d-axis and q-axis inductances according to (8), whose measured distributions are compared with the finite-element predictions in Fig. 21.

$$L_d\left(i_d, i_q\right) = \frac{\psi_d\left(i_d, i_q\right)}{i_d},\; L_q\left(i_d, i_q\right) = \frac{\psi_q\left(i_d, i_q\right)}{i_q} \qquad (8)$$

Unlike the flux-linkage maps and the MTPA trajectories, the apparent inductance distributions are considerably more sensitive to local variations of the measured flux-linkage surfaces, particularly at low current levels where small measurement uncertainties are amplified by the flux-to-current ratio. Nevertheless, the measured and simulated inductance maps exhibit good overall agreement for both prototypes, confirming the validity of the adopted electromagnetic model.

The comparison also reveals systematic discrepancies, particularly in the q-axis inductance, that cannot be fully explained by the manufacturing tolerances alone. These discrepancies are consistent with the presence of the interfacial diffusion region observed in the metallographic cross-section shown in Fig. 22. The metallurgical origin and characteristics of this interfacial region are discussed in [18], whereas its electromagnetic implications are experimentally investigated in [30].

C. EXPERIMENTAL TORQUE CAPABILITY VALIDATION

Following validation of the electromagnetic model using measured flux-linkage maps, MTPA trajectories, and apparent

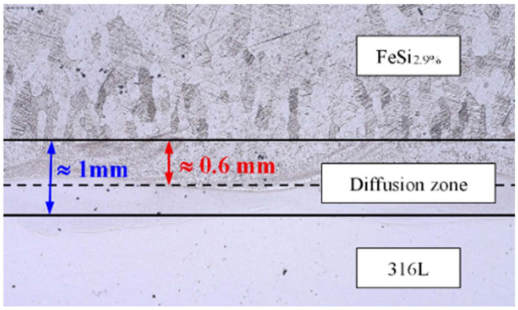

FIGURE 22. Etched microstructure of the interlayer dilution region between FeSi2.9% and AISI 316L.

TABLE 6. Prototype 1: Short-Time Overload Capability

Speed	Torque	CurrentAngle	Winding temp.	Vline,fund	Iline	Pinput	Eff.	PF
rpm	Nm	°	°C	V	A	W	-	-
24 998	0.050	45.0	58.3	39.08	4.216	188.7	0.699	0.608
25 000	0.100	46.0	80.3	53.0	6.016	369.3	0.709	0.629
25 003	0.150	47.6	86.6	62.4	7.548	552.2	0.712	0.644
25 003	0.201	49.6	79.4	69.1	9.006	736.7	0.713	0.656
50 000	0.050	45.0	70.3	75.57	4.221	352.7	0.739	0.586
50 000	0.100	46.0	87.2	101.7	6.051	676.6	0.775	0.603
50 004	0.149	47.6	95.9	118.5	7.560	989.4	0.791	0.615
50 010	0.199	49.5	85.0	129.5	8.979	1288.6	0.808	0.622

inductance distributions, the final step of the experimental campaign was to assess the ability of the two manufactured prototypes to deliver the mechanical performance predicted during the design stage. To this end, an extensive load-validation campaign was carried out over a wide operating range by means of both continuous (steady-state) and short-time overload tests. The steady-state measurements verify the capability of the machine to operate continuously within its thermal limits, whereas the overload tests assess the maximum torque that can be temporarily sustained under transient operating conditions.

The measured operating points were compared with the finite-element predictions presented in Section IV to experimentally validate the electromagnetic design over the complete operating range.

For Prototype 1, the experimental investigation was limited to a maximum speed of 75 krpm because of a defect in the carbon-fiber retaining sleeve of the PM loading machine employed in the first experimental setup. This limitation was exclusively related to the test bench and does not reflect any limitation of the proposed SynRM prototype or of its rotor design. Because the experimental test bench does not allow direct efficiency measurements, the efficiencies reported in this section were estimated from the measured operating points assuming optimum MTPA operation throughout the investigated speed–torque range. Consequently, the reported efficiency values should be regarded as estimated performance indices rather than directly measured quantities.

TABLE 7. Prototype 2: Steady-State Load Tests

Speed	Torque	CurrentAngle	Winding temp.	Vline,fund	Iline	Pinput	Eff.	PF
rpm	Nm	°	°C	V	A	W	-	-
25 000	0.100	48.5	76.2	65.5	5.999	382.4	0.683	0.519
50 000	0.098	48.4	88.2	126.3	5.982	685.3	0.750	0.494
74 983	0.099	48.5	93.9	187.7	6.125	1024	0.757	0.491
100 004	0.099	48.5	116.6	251.3	6.294	1408	0.734	0.495

TABLE 8. Prototype 2: Short-Time Overload Capability

Speed	Torque	CurrentAngle	Winding temp.	Vline,fund	Iline	Pinput	Eff.	PF
rpm	Nm	°	°C	V	A	W	-	-
24 999	0.051	46.4	60.0	49.7	4.105	193.3	0.685	0.486
24 999	0.101	48.6	79.6	66.1	6.030	386.7	0.681	0.517
25 002	0.150	51.2	92.9	76.1	7.653	578.7	0.680	0.541
25 007	0.210	54.8	111.8	84.4	9.426	805.0	0.683	0.559
49 996	0.051	46.4	69.4	97.6	4.161	366.3	0.731	0.469
50 000	0.100	48.5	93.9	127.6	6.039	695.5	0.751	0.493
50 005	0.149	51.1	102.9	144.7	7.651	1006	0.775	0.507
50 015	0.193	54.7	106.9	157.6	9.438	1355	0.748	0.514
75 003	0.050	46.3	70.2	141.5	4.135	510.8	0.761	0.471
75 003	0.099	48.5	90.7	186.8	6.084	984.6	0.790	0.489
75 007	0.148	51.1	98.8	211.3	7.721	1421	0.819	0.495
75 000	0.213	55.0	125.3	230.9	9.666	1964	0.851	0.502

The experimental results obtained for Prototypes 1 and 2 under continuous operating conditions are summarized in Tables 5 and 7, whereas the corresponding short-time overload capability is reported in Tables 6 and 8, respectively.

Overall, the experimental results demonstrate good agreement with the finite-element predictions over the investigated operating range. Both prototypes successfully achieve the expected operating points, confirming the capability of the proposed additively manufactured ALA rotor to deliver the mechanical output predicted during the design stage.

The remaining discrepancies are limited and are consistent with the modelling approximations discussed in the previous-section, particularly those associated with the finite diffusion region generated during the L-DED process. Although the diffusion region is expected to exhibit comparable dimensions in both prototypes, its relative influence becomes more pronounced in Prototype 2 because of the reduced thickness of the nonmagnetic layers. As a consequence, the diffusion region occupies a larger fraction of the nominal FB thickness, leading to a more significant impact on the effective electromagnetic behavior, particularly in terms of the estimated efficiency and the fundamental power factor.

It should also be noted that the efficiencies reported in Tables 5–8 are not directly measured quantities but estimates obtained assuming ideal MTPA operation throughout the investigated operating range. Consequently, these values are expected to become increasingly optimistic at high speed because the adopted MTPA trajectories do not account for the current-angle detuning introduced by the speed-dependent loss component [28]. Therefore, the reported efficiencies should be regarded as estimated performance indices rather than direct experimental measurements. The authors are currently developing a shaft torque estimation method based on

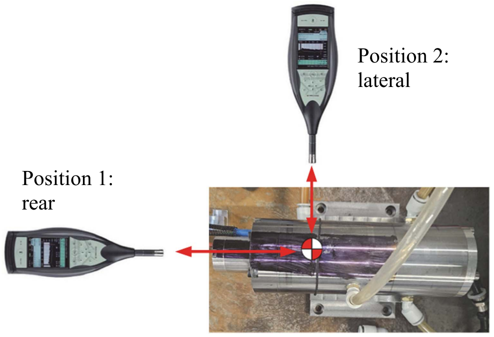

FIGURE 23. Experimental arrangement adopted for the sound-level measurement (position 1: rear side, position 2: lateral side).

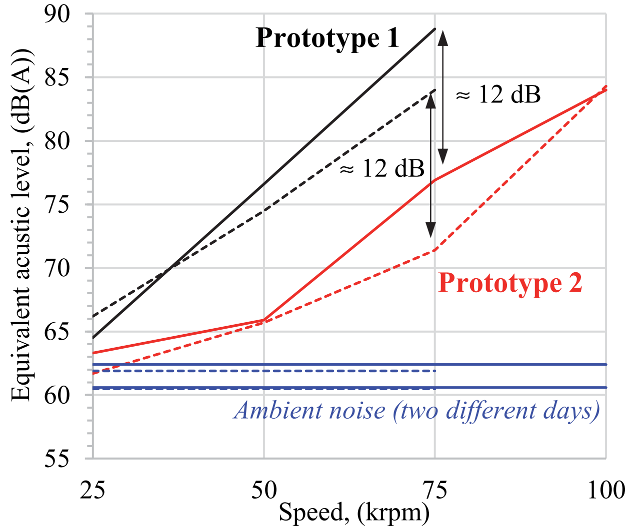

FIGURE 24. Equivalent A-weighted sound-pressure level measured for Prototype 1 and Prototype 2 (solid lines: position 1, dashed lines: position 2, blue lines: ambient-noise levels measured on two test days).

the power balance enabled by the test rig configuration shown in Fig. 18.

D. SOUND LEVEL MEASUREMENTS

A direct experimental measurement of torque ripple at rotational speeds approaching 100 krpm is not feasible with the available test bench. Therefore, an indirect assessment was carried out through acoustic-noise measurements. Since electromagnetic torque pulsations represent one of the excitation sources of high-speed synchronous reluctance machines [31], a reduction in the radiated acoustic noise can provide experimental evidence consistent with a reduction in the corresponding electromagnetic excitation.

The sound-level measurements were performed using the arrangement shown in Fig. 23. A calibrated sound-level meter (Brüel & Kjær, G-4, Type 2250) was placed approximately 95 cm from the machine in two positions: Position 1, facing the rear of the prototype, and Position 2, facing its lateral side. All measurements were carried out at rated torque with a fixed current angle of 45°, thereby ensuring comparable electromagnetic excitation conditions for the two prototypes. The measurements were repeated for both machines using the same test bench and under the same operating conditions.

The measured equivalent A-weighted sound-pressure levels are reported in Fig. 24. At rotational speeds up to approximately 50 krpm, the acoustic emissions of the two prototypes remain comparable and only moderately exceed the ambient-noise level. At higher speeds, however, the difference becomes progressively more evident. Prototype 2 exhibits lower sound levels than Prototype 1 in both measurement positions, with a reduction of approximately 10–12 dB(A) at 75 krpm.

Although the acoustic measurements do not provide a direct quantitative estimate of the electromagnetic torque ripple, the consistent reduction observed for Prototype 2 under identical test conditions is compatible with a lower level of electromagnetic excitation. This result provides independent experimental evidence supporting the effectiveness of the optimized rotor geometry and of the refined layer-grinding process adopted for the second prototype.

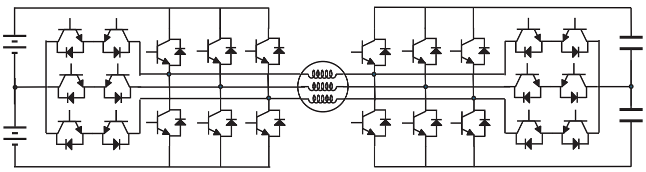

FIGURE 25. Dual-inverter configurations: two three-level T-type converters.

VI. TURBO POWER CONVERTER AND DRIVE CONTROL

A. DUAL-INVERTER CONVERTER TOPOLOGY

As shown in Fig. 25, the developed drive employs two three-phase, three-level T-type inverters, to feed the SynRM in an open-end winding configuration. This solution is well-suited to high-speed SynRM operation, where low power factor and rising stator voltage reduce the effectiveness of single-inverter solutions [32], [33], [34]. The open-end winding terminal voltage space vector is as follows:

$$\bar{v}_S = \bar{v}_A - \bar{v}_B \tag{9}$$

where $\bar{v}_A$ and $\bar{v}_B$ are the pole voltage space vectors of Inverters A and B. Inverter A, connected to the main dc source, primarily transfers active power. Inverter B injects an additional voltage through its floating-capacitor bridge, enabling reactive-power compensation, voltage boosting, and multilevel synthesis. This arrangement reduces the main-inverter dc-link voltage by approximately 30% compared to a single-inverter solution while extending the available speed range [33]. The voltage limits for space-vector modulation or PWM with third-harmonic injection are $V_{A,\max} = E_A/\sqrt{3}$ and $V_{B,\max} = E_B/\sqrt{3}$, where E_A and E_B are the total dc-link voltages, equal to 200 V and 250 V, respectively. Both inverters employ SiC devices switching at 30 kHz with a 400 ns dead time. The DC-link capacitors in series are 200 μF .

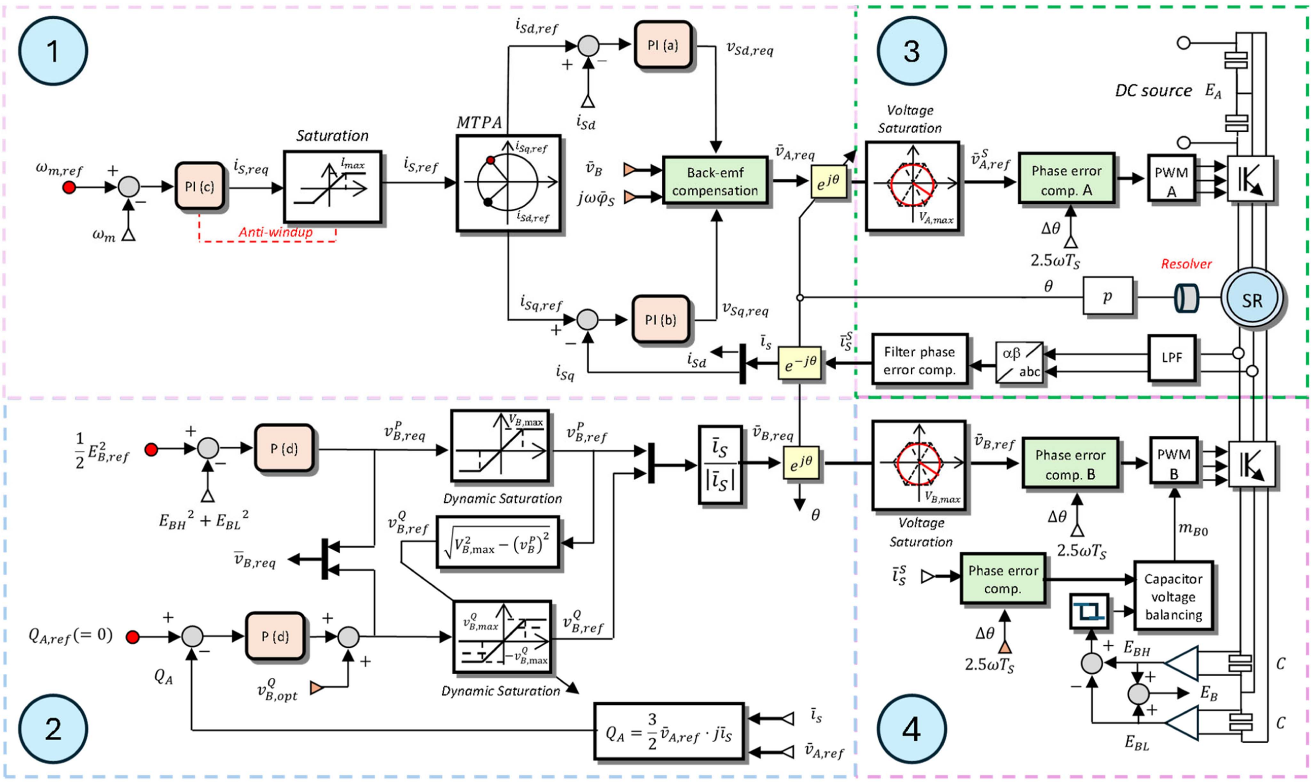

FIGURE 26. Overall control architecture of the proposed TUrBO open-end winding SynRM drive.

B. DRIVE CONTROL ARCHITECTURE

The machine is modelled in the rotor-synchronous d-q reference frame, with the d-axis aligned to the minimum-inductance axis. The stator-voltage equations are as follows:

$$v_d = R_s i_d - \omega\lambda_q + \frac{d\lambda_d}{dt} \tag{10}$$

$$v_q = R_s i_q + \omega\lambda_d + \frac{d\lambda_q}{dt}. \tag{11}$$

The overall control architecture (see Fig. 26) comprises speed and current control loops for Inverter A (see Section I), and reactive-power and floating-capacitor energy control loops for Inverter B (see Section II), with the corresponding modulation stages (see Sections III and IV). The field-oriented control architecture with MTPA current references is implemented in the synchronous *d*-*q* frame.

The control scheme is based on the decomposition of the output voltage of Inverter B into components parallel and orthogonal to the stator current vector as follows:

$$\bar{v}_B = \left(v_B^P + j v_B^Q\right) \frac{\bar{i}_S}{|\bar{i}_S|}. \tag{12}$$

The parallel component v_B^P determines active-power exchange and regulates floating-capacitor energy as follows:

$$\frac{1}{2} C \frac{d}{dt}\left(E_{BH}^2 + E_{BL}^2\right) = \frac{3}{2} v_B^P \left|\bar{i}_S\right|. \tag{13}$$

The orthogonal component v_B^Q controls the reactive power of Inverter A as follows:

$$Q_A = \frac{3}{2}\bar{v}_A \cdot j\bar{i}_S = Q_S + Q_B. \tag{14}$$

Imposing $Q_A = 0$ and neglecting stator resistance yields the required orthogonal component for unity-power factor operation as follows:

$$v_B^Q = -\frac{\omega\bar{\lambda}_S \cdot \bar{i}_S}{|\bar{i}_S|}. \tag{15}$$

This is the analytical basis for the TUrBO drive's key capability: the floating-capacitor inverter compensates for the machine reactive power, enabling the main inverter to operate at unity power factor.

At very high speed, if the required v_B^Q exceeds Inverter B's voltage capability, the bridge saturates as follows:

$$\bar{v}_B = -j\left(\text{sgn}\omega\right) V_{B,\max} \frac{\bar{i}_S}{\left|\bar{i}_S\right|}. \tag{16}$$

At high rotor speeds, the ratio between the switching frequency and the fundamental frequency (the frequency modulation index) becomes smaller. This reduction introduces predictable errors in the inverter's output voltage due to PWM behavior and delays in digital control. The average inverter output over one switching period can be approximated as a delayed and slightly attenuated version of the reference. When

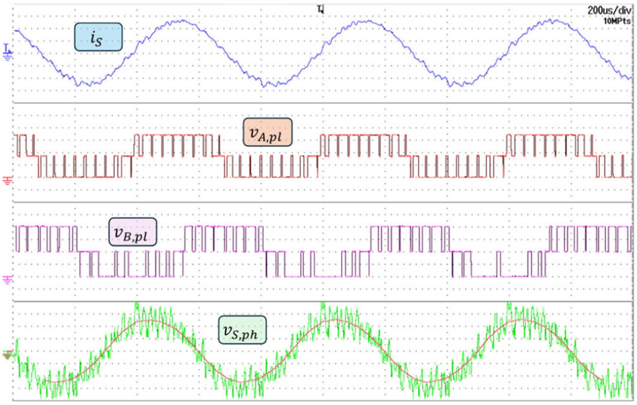

FIGURE 27. Steady-state no-load operation of the TUrBO drive at 100 krpm. From top to bottom: phase current (1 A/div), pole voltage of Inverter A (50 V/div), pole voltage of Inverter B (50 V/div), and phase voltage (50 V/div).

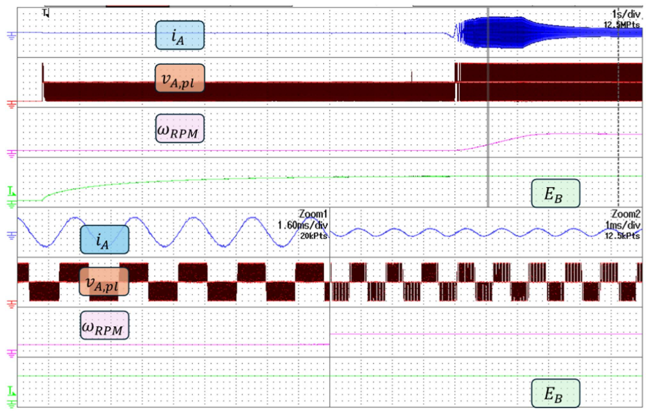

FIGURE 29. Start-up transient of the TUrBO motor up to 50 krpm. From top to bottom: phase current (2 A/div), pole voltage of inverter A (25 V/div), motor speed (20 krpm/div), DC-link voltage of inverter B (50 V/div).

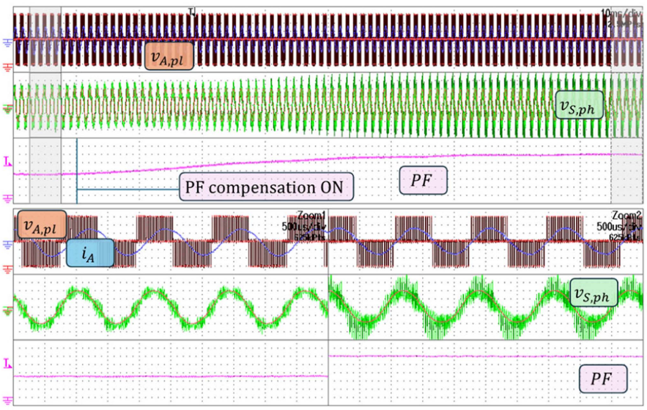

FIGURE 28. Measured response of the power-factor-compensation function at 50 krpm. From top to bottom: phase current and pole voltage of Inverter A, actual and filtered stator phase voltage, and input power factor.

additional delays from digital computation—typically equal to one or two switching periods—are included, the effective output voltage is further shifted in time.

To correct these effects, the reference voltage must be adjusted in advance: it is phase-shifted forward to counteract the delay and scaled to compensate for amplitude reduction. In practice, the amplitude correction factor is usually very close to one, so it is often ignored. As a result, only the phase compensation is typically applied [33].

The drive was validated using the 1 kW, 100 krpm TUrBO prototype. Fig. 27 shows steady-state no-load operation at 100 krpm. At steady state, the phase current is nearly sinusoidal with negligible ripple. The pole voltage of Inverter A is approximately in phase with the current (active-power role), while that of Inverter B is in quadrature (reactive-power role). The phase voltage exhibits a clear multilevel structure.

Fig. 28 shows the transient response when power-factor compensation is enabled at 50 krpm. Before activation, the power factor is approximately 0.5. After enabling compensation, it increases progressively toward unity, accompanied by alignment of Inverter A's pole voltage with the stator current, confirming the reactive-power-compensation capability predicted by (13)-(14). These results confirm the suitability of the dual-inverter architecture and coordinated control for high-speed PM-free SynRM operation.

Fig. 29 shows, from top to bottom, the phase current, the pole voltage of inverter A (first leg), the rotor speed, and the DC-link voltage of inverter B during motor start-up. Before the motor begins operating, the DC-link voltage E_B is precharged from zero to its rated value.

As the motor accelerates, the phase current rises to provide the required electromagnetic torque, then decreases as the system approaches steady state. Once steady conditions are reached, the current settles at a low level sufficient to compensate for friction losses. Meanwhile, the DC-link voltage of inverter B remains constant throughout the transient, demonstrating effective voltage regulation and energy control.

VII. CONCLUSION

This article presented the integrated conception, realization, and experimental validation of a PM-free synchronous reluctance drive capable of operation in the 100 krpm class. Rather than addressing the electrical machine and the power converter as independent subsystems, the proposed approach demonstrated that practical ultrahigh-speed SynRM operation requires the coordinated development of the rotor architecture, AM process, electromagnetic design, and converter topology.

The proposed multimaterial L-DED ALA rotor was shown to simultaneously satisfy the mechanical integrity and electromagnetic requirements imposed by ultrahigh-speed operation. The combination of finite-element analysis, mechanical verification, flux-linkage mapping, apparent inductance evaluation, MTPA assessment, load testing, and acoustic measurements provided a comprehensive experimental validation of the proposed machine. The comparison between simulations and measurements also highlighted the influence of manufacturing-specific phenomena, particularly the FeSi2.9/316L diffusion region, demonstrating that additive-manufacturing characteristics must be explicitly considered in the electromagnetic design of high-speed reluctance machines.

The experimental results further confirmed that the proposed open-end winding architecture provides a suitable platform for extending the operating range of high-speed synchronous reluctance drives while maintaining the advantages of a completely PM-free solution. The complete experimental campaign therefore demonstrates the feasibility of combining advanced AM and converter-assisted operation to achieve very-high-speed SynRM drives.

The presented results indicate that further improvements are expected through a more accurate modeling of the interfacial diffusion region and by further refinement of the multimaterial manufacturing process. Nevertheless, the proposed system-level methodology provides a practical framework for the development of the next generation of sustainable ultrahigh-speed electrical drives.

REFERENCES

[1] D. Gerada, A. Mebarki, N. L. Brown, C. Gerada, A. Cavagnino, and A. Boglietti, "High-speed electrical machines: Technologies, trends, and developments," *IEEE Trans. Ind. Electron.*, vol. 61, no. 6, pp. 2946–2959, Jun. 2014.

[2] Fortune Business Insights, "Turbocompressor market, 2021–2028," Rep. no. FBI101400, 2022. Accessed: Aug. 3, 2026. [Online]. Available: https://www.fortunebusinessinsights.com/industry-reports/turbocompressor-market-101400

[3] A. Borisavljevic, *Limits, Modeling and Design of High-Speed Permanent Magnet Machines*. Berlin, Germany, Springer-Verlag, 2012.

[4] N. Bianchi, S. Bolognani, and F. Luise, "Potentials and limits of high-speed PM motors," *IEEE Trans. Ind. Appl.*, vol. 40, no. 6, pp. 1570–1578, Nov./Dec. 2004.

[5] European Commission, "Report on critical raw materials for the EU," 2014, pp. 1–41. [Online]. Available: https://www.actu-environnement.com/media/pdf/news-23426-report-criticam-rax-materials-2014.pdf

[6] B. Poudel, E. Amiri, P. Rastgoufard, and B. Mirafzal, "Toward less rare-earth permanent magnet in electric machines: A review," *IEEE Trans. Magn.*, vol. 57, no. 9, Sep. 2021, Art. no. 900119.

[7] M. Murataliyev, M. Degano, M. D. Nardo, N. Bianchi, and C. Gerada, "Synchronous reluctance machines: A comprehensive review and technology comparison," *Proc. IEEE*, vol. 110, no. 3, pp. 382–399, Mar. 2022.

[8] E. Scherman et al., "Axially-laminated synchronous reluctance machine rotor materials and evaluation of manufacturing methods: Mechanical and electromagnetic validation," *IEEE Trans. Ind. Appl.*, vol. 61, no. 5, pp. 7141–7153, Sep./Oct. 2025.

[9] C. Gianassi et al., "Laser directed energy deposition of FeSi/SS 316L advanced bimetallic high-speed rotors: From material characterization to performance evaluation," *Adv. Ind. Manuf. Eng.*, vol. 11, Nov. 2025, Art. no. 100175.

[10] Y. Cui, C. Gianassi, A. Fortunato, L. Zarri, and A. Cavagnino, "High-speed synchronous reluctance motors with additively manufactured rotors," in *Proc. IEEE Energy Convers. Congr. Expo.*, 2024, pp. 5024–5031.

[11] D. Newman et al., "Development of solid synchronous reluctance rotors with multi-material additive manufacturing," *IEEE Trans. Ind. Appl.*, vol. 61, no. 2, pp. 2911–2923, Mar./Apr. 2025.

[12] D. Newman et al., "Solid high-speed synchronous reluctance rotor enabled by multi-material additive manufacturing," in *Proc. IEEE Energy Convers. Congr. Expo.*, 2023, pp. 3965–3972.

[13] J. Ikäheimo, J. Kolehmainen, T. Känsäkangas, V. Kivelä, and R. R. Moghaddam, "Synchronous high-speed reluctance machine with novel rotor construction," *IEEE Trans. Ind. Electron.*, vol. 61, no. 6, pp. 2969–2975, Jun. 2014.

[14] C. Gianassi, E. Liverani, A. Ascari, A. Tonoli, A. Cavagnino, and A. Fortunato, "Characterization of FeSi2.9 and SS 316L produced by directed energy deposition for bimetallic high-speed rotors," in *Proc. Int. Manuf. Sci. Eng. Conf.*, vol. 89022, 2025, Art. no. V002T13A002.

[15] Q. Xiao, J. Chen, H. B. Lee, C. Jang, and K. Jang, "Effect of heat treatment on corrosion behaviour of additively manufactured 316L stainless steel in high-temperature water," *Corrosion Sci.*, vol. 210, 2023, Art. no. 110830.

[16] A. Credo, E. Kurvinen, I. Petrov, E. Scherman, J. Sopanen, and J. Pyrhönen, "Materials applicable to an axially-laminated synchronous reluctance machine considering mechanical and electromagnetic aspects," *IEEE Trans. Ind. Appl.*, vol. 60, no. 1, pp. 153–163, Jan./Feb. 2024.

[17] Y. Cui, C. Gianassi, G. Rizzoli, A. Fortunato, L. Zarri, and A. Cavagnino, "Prototyping and optimization of 100,000 rpm additively manufactured SyR rotors," in *Proc. IEEE Energy Convers. Conf. Expo.*, 2025, pp. 1–7.

[18] C. Gianassi, E. Liverani, A. Cavagnino, and A. Fortunato, "Property tailoring in multi-material laser directed energy deposition of high-speed SynRel rotors," in *Proc. 14th CIRP Conf. Photon. Technol.*, 2026, vol. 143, pp. 66–69.

[19] Y. Cui, B. Mecrow, and A. Cavagnino, "Multidisciplinary design methodology for ultra-high-speed PM motors," in *Proc. Int. Conf. Elect. Mach.*, 2024, pp. 1–7, doi: 10.1109/ICEM60801.2024.10700555.

[20] I. Boldea and L. Tutelea, *Reluctance Electric Machines: Design and Control*. Boca Raton, FL, USA, CRC Press, 2018.

[21] T. A. Lipo, *Introduction to AC Machine Design*. Hoboken, NJ, USA, Wiley, 2017.

[22] A. Borisavljevic, H. Polinder, and J. A. Ferreira, "On the speed limits of permanent-magnet machines," *IEEE Trans. Ind. Electron.*, vol. 57, no. 1, pp. 220–227, Jan. 2010.

[23] G. Gallicchio et al., "High speed synchronous reluctance machines: Modeling, design and limits," *IEEE Trans. Energy Convers.*, vol. 37, no. 1, pp. 585–597, Mar. 2022.

[24] A. Vagati, M. Pastorelli, G. Franceschini, and S. C. Petrache, "Design of low-torque-ripple synchronous reluctance motors," *IEEE Trans. Ind. Appl.*, vol. 34, no. 4, pp. 758–765, Jul./Aug. 1998.

[25] J. E. Shigley, L. D. Mitchell, and H. Saunders, *Mech. Eng. Des.* Columbus, OH, USA:McGraw-Hill Sci. Eng., 1985.

[26] A. Gunduz and R. Singh, "Stiffness matrix formulation for double row angular contact ball bearings: Analytical development and validation," *J. Sound Vib.*, vol. 332, no. 22, pp. 5898–5916, 2013.

[27] E. Gargiulo, "A simple way to estimate bearing stiffness," *Mach. Des.*, vol. 52, no. 17, pp. 107–110, 1980.

[28] G. Rizzoli, M. Mengoni, L. Zarri, Y. Cui, and A. Cavagnino, "MTPA experimental validation of 100+ krpm SynRel motors without torque measurements," in *Proc. IEEE Energy Convers. Congr. Expo.*, 2026, pp. 1–8.

[29] E. Armando, R. I. Bojoi, P. Guglielmi, G. Pellegrino, and M. Pastorelli, "Experimental identification of the magnetic model of synchronous machines," *IEEE Trans. Ind. Appl.*, vol. 49, no. 5, pp. 2116–2125, Oct. 2013.

[30] Y. Cui, G. Rizzoli, L. Zarri, C. Gianassi, A. Fortunato, and A. Cavagnino, "Experimental-based inductance map refinement of a 100 krpm SyR motor equipped with 3D-printed bimetallic rotors," in *Proc. IEEE Energy Convers. Congr. Expo.*, 2026, pp. 1–8.

[31] J. F. Gieras, C. Wang, and J. C. Lai, *Noise of Polyphase Electric Motors*. Boca Raton, FL, USA, CRC Press, 2018.

[32] R. Testa et al., "Open-end winding SyncRel motor drive with a floating capacitor bridge for high-speed applications," in *Proc. IEEE Energy Convers. Congr. Expo.*, 2024, pp. 6163–6169.

[33] D. S. Nayak, G. Rizzoli, M. Mengoni, L. Zarri, A. Tani, and A. Cavagnino, "100+ krpm open-end winding reluctance motor drive with a floating capacitor bridge," in *Proc. IEEE Energy Convers. Conf. Expo.*, 2025, pp. 1–7.

[34] Z. Huang, T. Yang, P. Giangrande, S. Chowdhury, M. Galea, and P. Wheeler, "Enhanced performance of dual inverter with a floating capacitor for motor drive applications," *IEEE Trans. Power Electron.*, vol. 36, no. 6, pp. 6903–6916, Jun. 2021.

YULONG CUI (Graduate Student Member, IEEE) received the M.Sc. degree in electrical engineering from Newcastle University, Newcastle, U.K., in 2023. He is currently working toward the Ph.D. degree with Politecnico di Torino, Torino, Italy.

His research interests include the design and analysis of high-speed electrical machines, with a focus on electromagnetics, mechanical stress, and rotordynamics.

ANDREA CAVAGNINO (Fellow, IEEE) received the Ph.D. degree in electrical engineering from the Politecnico di Torino, Torino, Italy, in 2000.

He is currently a Professor with the Politecnico di Torino. He has authored or coauthored more than 300 papers. He usually collaborates with factories on direct technology transfer, and he has been involved in several public and private research projects. His research interests include electromagnetic design, thermal design, and energetic behavior of electrical machines.

Dr. Cavagnino was the recipient of four Best Paper Awards. He is an Associate Editor of IEEE Transactions on Industry Applications.

ANDREA TONOLI received the Ph.D. degree in machine design from the Politecnico di Torino, Torino, Italy, in 1994.

He is currently a Professor with the Mechanical and Aerospace Engineering Department, Politecnico di Torino, Torino, Italy. He was the Founder of the Mechatronics Laboratory, Politecnico di Torino, and the Coordinator of the Spoke 2 (Sustainable Road Vehicle) of the National Sustainable Mobility Center (MOST). His research interests include active, passive, and regenerative shock absorbers, powertrain hybridization and energy management, rotordynamics, and active and passive magnetic bearings.

CHIARA GIANASSI received the M.Sc. degree in mechanical engineering from the University of Bologna, Bologna, Italy, in 2023 where she is currently working toward the Ph.D. degree in automotive engineering for intelligent mobility.

Her research interests include laser-based manufacturing technologies and metal additive manufacturing, with particular emphasis on directed energy deposition (DED).

ALESSANDRO FORTUNATO received the M.Sc. degree in mechanical engineering and the Ph.D. degree in mechanics of materials and manufacturing processes from the University of Bologna, Bologna, Italy, in 2000 and 2006, respectively.

He is currently a Full Professor in manufacturing technology with the University of Bologna, where he directs the mechanical engineering degree programs and the Centre of Advanced Laser Manufacturing. He has extensive experience in technology transfer and has led numerous industrial research projects. He is cofounder of the university spin-off Nextema and a member of the Ph.D. board in Automotive Engineering for Intelligent Mobility, the University of Bologna. He is actively involved in European research initiatives. His research interests include laser material processing, additive manufacturing, and laser–matter interactions.

Dr. Fortunato serves as an Associate Editor for journals in manufacturing and laser technologies..

ALESSANDRO ASCARI received the M.Sc. and Ph.D. degrees in mechanical engineering from the University of Bologna, Bologna, Italy, in 2005 and 2014, respectively.

He is currently an Associate Professor with the Department of Industrial Engineering, University of Bologna. He has been teaching manufacturing technology at the University of Bologna for more than 15 years. He has coauthored more than 80 international publications recognized on the most well-known platforms for scientific research monitoring and two textbooks. His research interests include industrial applications of lasers, with particular emphasis on welding processes of dissimilar materials, high-speed cutting processes of thin foils, and surface treatments based on cladding and transformation hardening.

ERICA LIVERANI received the M.Sc. degree in mechanical engineering and the Ph.D. degree in mechanics and advanced engineering sciences from the University of Bologna, Bologna, Italy, in 2013 and 2017, respectively.

She is currently an Associate Professor of manufacturing technology with the University of Bologna. She is involved in several national and international research projects and collaborates with local companies on industry-oriented research activities. Her research interests include laser-based processes, particularly metal additive manufacturing, cutting, and welding for EV applications, combining both experimental and modeling expertise.

DEEKSHITHA SRINIVAS NAYAK (Member, IEEE) received the Ph.D. degree in electrical and electronics engineering from the Manipal Institute of Technology, Manipal Academy of Higher Education, Udupi, India, in 2022.

She is currently a Postdoctoral Researcher with the Department of Electrical, Electronic, and Information Engineering, University of Bologna, Bologna, Italy. She has authored and coauthored several journal and conference papers, as well as book chapters, in the fields of power electronics and smart energy systems. Her research interests include electric drives, control of high-speed machines, renewable energy systems, and Internet of Things (IoT) applications.

GABRIELE RIZZOLI (Member, IEEE) received the M.Sc. and Ph.D. (Hons.) degrees in electrical engineering from the University of Bologna, Bologna, Italy, in 2012 and 2016, respectively.

He is currently an Assistant Professor with the Department of Electrical, Electronic, and Information Engineering “G. Marconi,” University of Bologna. His research interests include the design of electrical machines and the development and control of high-efficiency power converters for automotive and renewable energy applications.

MICHELE MENGONI (Senior Member, IEEE) received the M.Sc. (with honors) and Ph.D. degrees in electrical engineering from the University of Bologna, Bologna, Italy, in 2006 and 2010, respectively.

He is currently an Associate Professor with the Department of Electrical, Electronic and Information Engineering "G. Marconi," University of Bologna. His research interests include the design, analysis, and control of three-phase electric machines, multiphase drives, and ac/ac matrix converters.

Dr. Mengoni is currently an Associate Editor for IEEE Transactions on Industrial Electronics and IEEE Transactions on Industry Applications.

LUCA ZARRI (Senior Member, IEEE) received the M.Sc. and Ph.D. degrees in electrical engineering from the University of Bologna, Bologna, Italy, in 1998 and 2007, respectively.

Currently, he is a Full Professor of power electronics, electrical machines, and drives with the Department of Electrical, Electronic, and Information Engineering “Guglielmo Marconi,” University of Bologna. He has authored or coauthored more than 200 scientific papers. His research interests include the control of power converters and electric drives.

Dr. Zarri is a senior member of the IEEE Industry Applications, IEEE Power Electronics, and IEEE Industrial Electronics Societies. Currently, he is the Vice Chair of the IAS Industrial Power Conversion System Department.